

PAPER

Hollow pellet injection for magnetic fusion

To cite this article: Zhehui Wang *et al* 2019 *Nucl. Fusion* **59** 086024

View the [article online](#) for updates and enhancements.



IOP | ebooksTM

Bringing together innovative digital publishing with leading authors from the global scientific community.

Start exploring the collection—download the first chapter of every title for free.

Hollow pellet injection for magnetic fusion

Zhehui Wang¹, M.A. Hoffbauer¹, E.M. Hollmann², Z. Sun^{3,4}, Y.M. Wang³,
N.W. Eidietis⁵, Jiansheng Hu³, R. Maingi⁴, J.E. Menard⁴ and X.Q. Xu⁶

¹ Los Alamos National Laboratory, Los Alamos, NM 87545, United States of America

² University of California—San Diego, La Jolla, CA 92093, United States of America

³ Institute of Plasma Physics, Chinese Academy of Sciences, Hefei, AH 230031, China

⁴ Princeton Plasma Physics Laboratory, Princeton, NJ 08544, United States of America

⁵ General Atomics, PO Box 85608, San Diego, CA 92186-5608, United States of America

⁶ Lawrence Livermore National Laboratory, Livermore, CA 94550, United States of America

E-mail: zwang@lanl.gov

Received 23 January 2019, revised 28 March 2019

Accepted for publication 16 April 2019

Published 27 June 2019



CrossMark

Abstract

The precise delivery of mass to burning plasmas is an area of growing interest in magnetic fusion (MF). The amount of mass that is necessary and sufficient can vary depending on such parameters as the type of atoms involved, the type of applications, plasma conditions, mass injector, and injection timing. Motivated by edge localized mode (ELM) control in H-mode plasmas, disruption mitigation and other applications in MF, we report the progress and new possibilities in mass delivery based on hollow pellets. Here, a hollow pellet refers to a spherical shell mass structure with a hollow core. Based on an empirical model of pellet ablation, coupled with BOUT++ simulations of the ELM triggering threshold, hollow pellets are found to be attractive in comparison with solid spheres for ELM control. By using hollow pellets, it is possible to tailor mass delivery to certain regions of edge plasmas while minimizing core contamination and reducing the total amount of mass needed. We also include the experimental progress in mass delivery experiments, *in situ* diagnostics and hollow pellet fabrication, and emphasize new experimental possibilities for ELM control based on hollow pellets. A related application is the disruption mitigation scheme using powder encapsulated inside hollow shells. Further experiments will also help to resolve known discrepancies between theoretical predictions and experiments in using mass injection for ELM control and leading to better predictive models for ELM stability and triggering.

Keywords: hollow pellet, ELMs control, boron

(Some figures may appear in colour only in the online journal)

1. Introduction

One of the latest applications of mass injection in magnetic fusion (MF) is edge localized mode (ELM) control. ELMs are a key signature of high-confinement or H-mode plasmas. An H-mode plasma has a steep edge plasma pressure gradient and a spontaneous bootstrap current. The shear in the $\mathbf{E} \times \mathbf{B}$ flow near the edge pedestal provides a transport barrier to improve particle and energy confinement. The same pressure gradient and current give rise to natural ELMs and other MHD instabilities. The amount of energy released by ELMs is proportional to the stored plasma energy and can exceed 10% in extreme cases. Natural ELMs in ITER and similar can potentially accelerate the plasma facing wall deterioration,

and ELM control is therefore necessary for ITER and future fusion reactors [1–7]. Cryogenic hydrogen pellets [8] and impurity pellets have experimentally shown to be feasible in inducing ELMs at a frequency higher than the natural ELM frequency of a few Hz and can reduce the peak energy flux onto the divertor and other plasma-facing surfaces. Three-dimensional edge magnetic fields do not induce ELMs at higher than natural frequencies as per the pellet technique, but usually reduce the ELM frequency (hopefully to 0) and magnitude. Experimental results from JET, AUG, DIII-D, EAST and others have indicated that ELM suppression and triggering depend on the amount of mass injected. Cryogenic deuterium pellets and impurity pellets of lithium (Li) have been used experimentally. Only a sufficiently large Li pellet

(>600 μm in diameter) is able to trigger ELMs with 100% certainty in EAST [10, 11].

A number of questions remain open from both physics and technology perspectives regarding ELM control using mass injection. From a physics viewpoint, the complex interactions of the injected mass with large gradients near the plasma edge make the modeling and quantitative predictions difficult. Although qualitative agreement has been achieved between experiments and modeling, quantitative prediction of the mass ablation rate and pellet penetration depth are yet to be obtained, particularly for impurity pellets. For example, there are discrepancies between simulations such as JOREK and ELM pacing experiments using pellets in terms of the triggering threshold and triggering location [12, 13]. From a technology point of view, questions related to mass injection include the amount of mass needed, the timing of the mass injection with respect to the natural ELM cycle and location of the mass injection with respect to the magnetic flux surfaces and the edge pedestal, correlations between the injected mass properties with an induced ELM amplitude, and the size of the ELM heat flux footprint on the divertor and other plasma-facing surfaces. Additional experiments, together with modeling and injection technology improvements, will be required to further advance the mass injection for ELM control, and under different plasma conditions.

In this paper, we examine hollow pellet injection for ELM control in MF. Here, a hollow pellet refers to a spherical shell structure surrounding a hollow core. Most of the pellets used in MF, including cryogenic fueling and impurity pellets for ELM control, are objects topologically equivalent to a solid sphere. A shell structure surrounding an impurity mass, such as tungsten in the core, has been demonstrated as the TESPEL diagnostic [9]. A shell structure enclosing boron (B) powder has recently been demonstrated in DIII-D for disruption mitigation [14]. Compared with the existing mass injection techniques, hollow pellet injection is attractive for ELM control in the following ways: ELMs can be triggered while substantial impurity contamination to the plasma core can be avoided. Initial demonstration of hollow pellet injection may use various existing injectors. In addition to ELM control, the development of hollow pellets can enrich the pellet options for shell pellets, and applications in MF include disruption mitigation, diagnostics, wall conditioning, helium ash removal, impurity transport, etc.

The rest of the paper is organized as follows: we first present a theoretical model for pellet interactions with a H-mode plasma. The model is characterized by a number of parameters for the edge plasma condition, ablation, and ELM triggering threshold. Then the model is applied to Li and B pellets with a solid core and with a hollow core. Core impurity contamination is then compared for different pellet sizes, shell thicknesses, and pellet injection velocities. Prototype layered structures of B and polymers are fabricated and characterized. Experimental progress for hollow pellet injection using the existing technologies for solid pellets are discussed. A dual-filter imaging technique, which belongs to a class of spectral imaging techniques that can be selectively tailored to at least

two characteristic wavelengths, can be used for further development and applications of hollow pellet injection in MF.

2. ELM triggering and ablation models

ELM triggering involves multiple physical processes. We may separate the triggering process into pellet ablation, neutral atom ionization, cold plasma propagation, plasma thermalization, MHD mode growth, and an ELM crash, taking advantage of the separations in the temporal scales involved in ELM triggering. We will focus on two types of impurity pellets, namely Li and B, partially motivated by ongoing research using these materials in different forms and their additional benefits to wall conditioning in high-temperature plasma devices.

2.1. Ablation models

Plasma ablation of a pellet leads to the formation of a neutral cloud, which is subsequently ionized. The ionized atoms from a pellet propagate along the local magnetic flux tubes, justifying the assumption that the initial mass deposition is local to a flux tube in magnetized plasma. However, subsequent evolution of the ablation cloud can be quite complicated due to cloud polarization [15], $\mathbf{E} \times \mathbf{B}$ effect [16]. For a hydrogen pellet, the radial displacement is the strongest. For carbon and other atoms, the displacement may be less [17]. The simplified model used here ignores the radial displacement. The amount of mass deposited onto the flux tube is given by

$$N_{ab}(r) = \int \frac{dN}{dt} dt = \left\langle \frac{dN}{dt} \right\rangle \frac{\Delta}{v_p} = \left\langle \frac{dN}{dr} \right\rangle \Delta, \quad (1)$$

where $\langle dN/dt \rangle$ is the flux-tube-averaged ablation rate, Δ the width of the flux tube and v_p the pellet speed. v_p is assumed to be a constant determined at the injector, which ignores the rocket effect. The average ablation rate dN/dt (we remove the averaging ' $\langle \cdot \rangle$ ' symbol from now on for simplicity) can be in general written in the form [18, 19]

$$\frac{dN}{dt} = K n_{e0}^{k_1} T_{e0}^{k_2} r_p^{k_3}, \quad (2)$$

where the coefficient K and the exponents k_1 , k_2 , k_3 for electron density n_{e0} (prior to the pellet ablation), temperature T_{e0} (prior to the pellet ablation) and pellet radius r_p at the time of ablation depends on the microphysics of ablation as well as the material properties, such as the atomic number, ablation energy per atom, etc. Different empirical values for K and k_i ($i = 1-3$) have been proposed [18, 19] and we show a few of them for a H-mode plasma in figure 1.

The cryogenic-hydrogen-pellet-like neutral gas shielding (NGS) model gives the deepest penetration. A weak NGS model with a magnetically shaping coefficient of $f_B = 0.8$ gives the second deepest penetration, followed by the weak NGS model with no magnetic-field-shaping factor or $f_B = 1.0$, followed by a bare pellet model without any shielding. The fastest ablation or the shallowest penetration is for an enhanced ablation modeling as expected. In spite of their quantitative differences, as indicated in figure 1, the predictions of mass

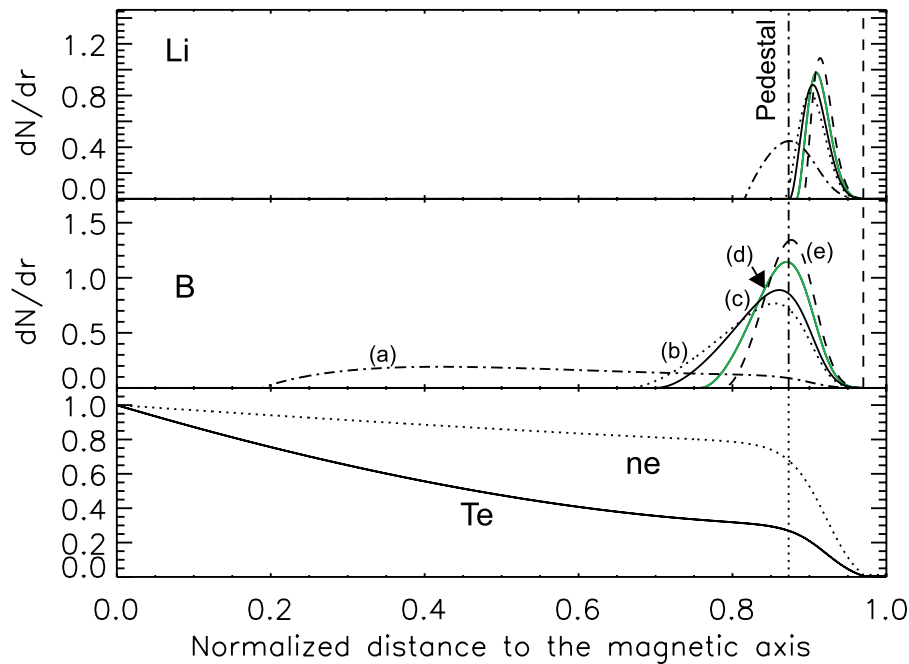


Figure 1. A comparison of various impurity pellet ablation models for dN/dr (in the unit of 10^{22} m^{-1}) as a function of the normalized minor radius. The fixed plasma temperature and density profiles, normalized to their core values ($T_e^{\text{max}} = 5 \text{ keV}$, $n_e^{\text{max}} = 8 \times 10^{19} \text{ m}^{-3}$), are shown for a H-mode plasma in the bottom frame. In the top and middle frames for Li and B respectively, the plotting symbols are matched for five models and ordered according to the pellet penetration distance from the deepest to the shallowest as: NGS model (a), weak NGS model with a magnetic-field shaping factor of 0.8 (b), weak NGS model (c), bare pellet model without shielding (d) and enhanced pellet ablation model (e). The normalized electron density and temperature profiles (with respect to the peak temperature and density) are shown in the bottom frames. The pellet initial radius is 1 mm and the initial velocity is 100 m s^{-1} . The separatrix density (the vertical line that is not labelled) is 10^{18} m^{-3} at a temperature of 30 eV. The pedestal width is 2% of the minor radius.

deposition for different models are qualitatively similar. Below, we use the weak NGS model without the magnetic-field shaping effect to examine the hollow pellet injection and compare it with solid pellet injection, consistent with earlier choices [18, 19].

2.2. ELM triggering mechanism and threshold

In the linear ideal MHD model, an ELM is triggered when the peeling–ballooning mode becomes unstable and leads to a growth rate $\gamma > \omega_*/2$ [20]. In the nonlinear models and simulations [21, 22], the triggering threshold becomes $\gamma > \gamma_c$, with $\gamma_c \sim 0.1/\tau_A$ and τ_A being the Alfvén time. Furthermore, JOREK simulations also showed that ELM triggering by pellet injection is correlated with the toroidally localized high edge pressure regions when the localized particle density increases due to the pellet ablation [23, 24]. A subsequent increase in pressure is due to ionized pellet particle heating by the ambient plasma. Recent simulations using BOUT++ arrived at similar conclusions [25]. When the pressure in this localized edge region exceeds a threshold, ballooning modes grow non-linearly leading to an ELM crash. In addition, the effects of the local electric field cannot be ignored. In short, the simulations and experimental evidence motivate an ELM triggering threshold in the total number of atoms (N_{th}) through

$$N_{\text{th}} = N(a_0, R_0, \Delta, n_{e0}, T_{e0}, Z, \dots), \quad (3)$$

where a_0 is the minor radius, R_0 is the major radius, Δ the radial width of the ablation cloud, as given in equation (1), n_{e0} and T_{e0} the local electron density and temperature before the pellet ablation, and Z is the atomic number of a single-element pellet, etc. In other words, such a threshold likely depends on the tokamak geometry, plasma parameters, and pellet material properties. Additional simulations and experimental data will be required to obtain a more precise function for N_{th} . Below, we shall assume the existence of a local N_{th} for the analysis of the hollow pellet injection concept.

3. Mass delivery and core impurity

In an ITER type-I ELMy H-mode plasma, electron density and temperature are $4 \times 10^{19} \text{ m}^{-3}$ and 500 eV respectively at the separatrix, and $8.7 \times 10^{19} \text{ m}^{-3}$ and 4 keV respectively at the top of the transport barrier. For comparisons of hollow and solid pellets, we use a H-mode profile that may be achieved in the existing devices to examine ELM triggering and theoretical predictions. Li and B pellets are compared here. The theoretical framework introduced can be readily extended to ELM triggering scenarios using other types of pellet materials and different plasma conditions.

In figure 2, the mass deposition as a function of normalized distance is shown for Li and B pellets with an initial radius of 1 mm and an injection velocity of 100 m s^{-1} . Two vertical dashed lines in the top frames mark the boundaries of the

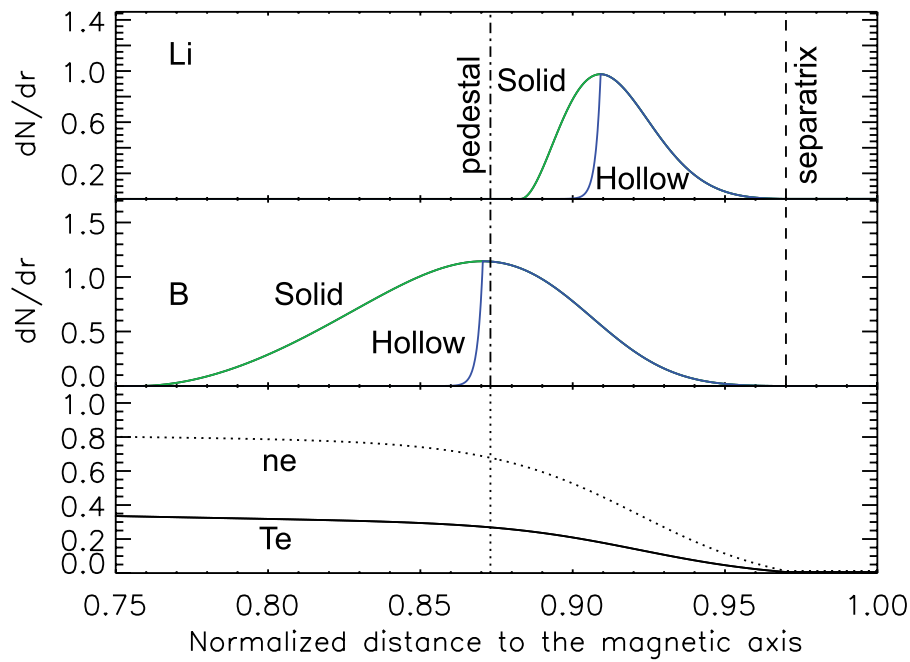


Figure 2. Comparison of the mass deposition of a solid-core pellet to that of a hollow pellet. The plasma condition is the same as in figure 1 and shown in the bottom frame. The pellet ablation dN/dr (in the unit of 10^{22} m^{-1}) for Li and B are shown in the top and middle frame respectively. A weak NGS model is used here. Other ablation models shown in figure 1 give qualitatively similar results. The normalized electron density and temperature profiles (with respect to the peak temperature and density) are shown in the bottom frame. Hollow pellets can achieve similar peak mass deposition while minimizing core plasma contamination. The pellet initial radius is 1 mm, and the initial velocity is 100 m s^{-1} . The hollow Li and B pellets have a shell thickness of around $260 \mu\text{m}$ and $170 \mu\text{m}$ respectively.

pedestal region as in figure 1. In contrast with solid pellets, a sharper decrease in mass deposition after the ablation rate reaches its maximum is expected for both Li and B hollow pellets. For solid pellets, the deeper deposition of B inside the pedestal top is due to the combination of two factors: its higher ablation energy per atom and larger number of atoms for a fixed size (about $3\times$ larger). The average energy of ablation used here is $5.6 \pm 0.6 \text{ eV}$ per B atom and $1.6 \pm 0.4 \text{ eV}$ per Li atom, consistent with previous estimates [18, 19]. The strong dependence of the mass deposition on the ablation energy per atom is also confirmed with a cryogenic hydrogen pellet of the same size (ablation energy 5.3 meV per atom [18, 19]), which reaches its peak of mass deposition at a shallower depth than both the Li and B pellets.

The results in figure 2 are consistent with earlier findings demonstrating that, in order to reliably trigger an ELM, the pellet needs to be sufficiently large (and fast) to penetrate close to the pedestal top [12, 13, 26]. Although both solid and hollow pellets can trigger ELMs, the fact that ELM triggering is near the top of the pedestal potentially poses an issue of core contamination using impurity pellets, as implied by figure 2. Strong atomic number (Z)-dependence of the core contamination may be expected when using impurity pellets for ELM control.

3.1. Core impurities

It is necessary to minimize the core impurity buildup when using mass injection or other methods for ELM pacing and control [5]. The impurities can come from a number of

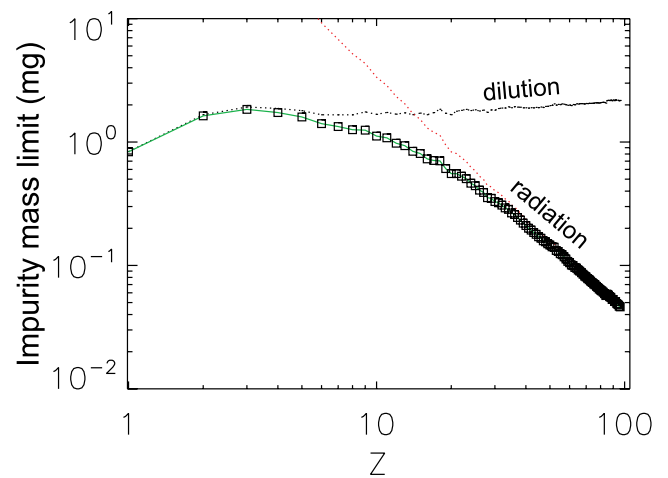


Figure 3. The mass limits (in mg) for different elements using impurity fraction limits bound by dilution and radiation ('□' symbol). The two dashed lines (color coded online) correspond to the dilution and radiation limit respectively. The mass limit for Li is 1.84 mg (0.94 mm in a solid sphere radius), and for B is 1.60 mg (0.55 mm in a solid sphere radius). The total number of plasma electrons is assumed to be 1.0×10^{22} .

sources: the impurity pellets themselves, impurities released from the wall and divertor due to the heat and particle fluxes from ELMs, and DT fusion generated helium. The impurity mass limits have been estimated as a function of the atomic number (Z) using the known processes of dilution for low- Z and radiation for high- Z impurities [27]. A quantitative result using a similar empirical formula is given in figure 3 for the total number of plasma electrons of 1.0×10^{22} . For sufficiently

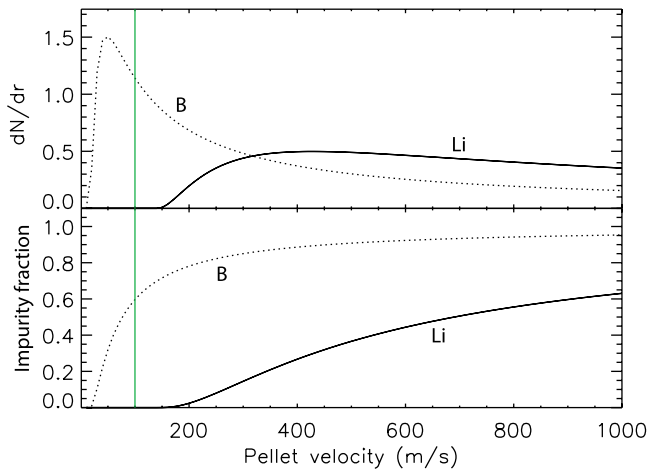


Figure 4. For a fixed pellet radius of $r_p = 1$ mm and fixed pedestal conditions as in figure 2, (top) the mass deposition (dN/dr in 10^{22} m^{-1}) as a function of Li or B solid sphere injection velocity. (Middle) The fraction of the solid spheres that reach beyond the ELM triggering location as a function of injection velocity. The colored vertical line corresponds to the example shown in figure 2.

small Z , the fraction of the atoms due to fuel dilution is limited to $0.05/Z$ of the total number of fuel ions or electrons. For example, the hydrogen (^1H) concentration should not exceed 5% of the electron density in the plasma. Helium fraction, including contributions from the fusion process, should be kept below 3%. For high- Z atoms such as tungsten, the concentration is limited to $10/Z^3$ or 2.5×10^{-5} . Each ELM event is known to expel impurities from the plasma and to mitigate the buildup of plasma core impurities, although how far inside the separatrix the impurities are expelled during the ELMs needs further study. The potential advantages of a hollow pellet that can trigger ELMs while minimizing the core impurity deposition warrant further experimental validation.

3.2. Velocity and size dependence

We further examine the mass deposition from solid pellets as a function of initial size and injection velocity. For simplicity, we shall consider pellet penetration at a constant initial injection velocity and ignore acceleration due to ablation and other plasma–pellet interactions. We also assume that ELM triggering occurs at a fixed minor radius. Specifically, at the location near the shoulder of the pedestal top, or the normalized minor radius at 0.87 as shown in figure 2. The corresponding local electron temperature and density are 1.3 keV and $6.3 \times 10^{19} \text{ m}^{-3}$. Similar to figure 2 for a fixed pellet radius of 1 mm, the mass deposition as a function of pellet injection velocity is shown in figure 4.

The trends in mass deposition are similar for Li and B. A peak deposition is reached near 50 m s^{-1} for B and 450 m s^{-1} for Li. A significant amount of mass deposition is expected following the ablation at the targeted radius of 0.87 for high injection speeds and the amount increases with the injection velocities, as shown in the lower frame in figure 4. Reduction of the impurity using hollow pellets of the same initial radius of 1 mm is shown in figure 5. Furthermore, the observation

that a relatively flat or plateau region between $200\text{--}800 \text{ m s}^{-1}$ exists for B implies that a hollow pellet may also relax the requirements on the precise injection velocity for impurity control.

A number of existing impurity launchers may be used to achieve the injection speeds as required in figures 4 and 5 [7]. Different launchers may be distinguished by their different forces of acceleration. We would like to mention that the mechanical strength of the pellets may limit the maximum force of acceleration, in particular for thin hollow pellets [28]. A remedy is to increase the launcher size to accommodate a long pathlength of acceleration. Furthermore, a thin shell pellet may open doors to alternative acceleration methods, such as electrostatic acceleration, that are currently not in use for MF.

For a fixed pellet injection velocity of 100 m s^{-1} , the mass deposition as a function of pellet radius is shown in figure 6. The mass deposition increases with the pellet size, as expected. Meanwhile, the impurity fraction that can contaminate the plasma core also increases. In figure 7, the vertical lines correspond to the limits set by figure 3 for B and Li. The hollow pellet structure allows a wider radius selection than a solid structure within the impurity limits.

3.3. Optimal hollow pellet dimensions

Based on the above, the dimensions of an optimal spherical hollow pellet at a fixed injection velocity v_p , i.e. its initial radius and thickness, are determined by the following factors: the pedestal plasma condition, the amount of mass required to trigger an ELM, the tolerable impurity levels, and the atomic number (Z). As mentioned above, material strength also needs to be considered for hollow pellet injection, which may limit the launcher selections and acceleration methods when high injection speed is required at a short acceleration path length. The total hollow pellet mass is thus given by

$$M_h = M_1 + M_2 + M_3, \quad (4)$$

where $M_1 = N_{\text{th}}m_0$ is determined by the ELM triggering threshold, with N_{th} given by equation (3) and m_0 the atomic mass of the pellet. Pellets of chemical compounds can use the molecular mass instead of m_0 for an atomic mass. M_2 is the mass loss before the pellet reaches the targeted ELM triggering location, which is partially determined by the pedestal plasma condition. M_3 is the residual pellet mass passing through the targeted ELM triggering location, which is limited by the impurity tolerance level and ideally $M_3 = 0$. In the case studies, as in figure 2, M_2 sets the lower bound in the hollow shell thickness, and does not contribute to the ELM triggering. According to equation (1), M_1 can be related to the ablation rate as

$$\frac{M_1}{m_0} \equiv N_{\text{th}} = \frac{dN}{dr} \Delta = \kappa_2(r_p - T_h) \frac{dN}{dr}. \quad (5)$$

Here we use $\Delta = \kappa_2(r_p - T_h)$ with the dimensionless multiplier $\kappa_2 > 1$ that relates the ablated cloud width Δ and the instantaneous pellet size ($r_p - T_h$) at the ELM triggering location. T_h represents the pre-triggering shell thickness loss.

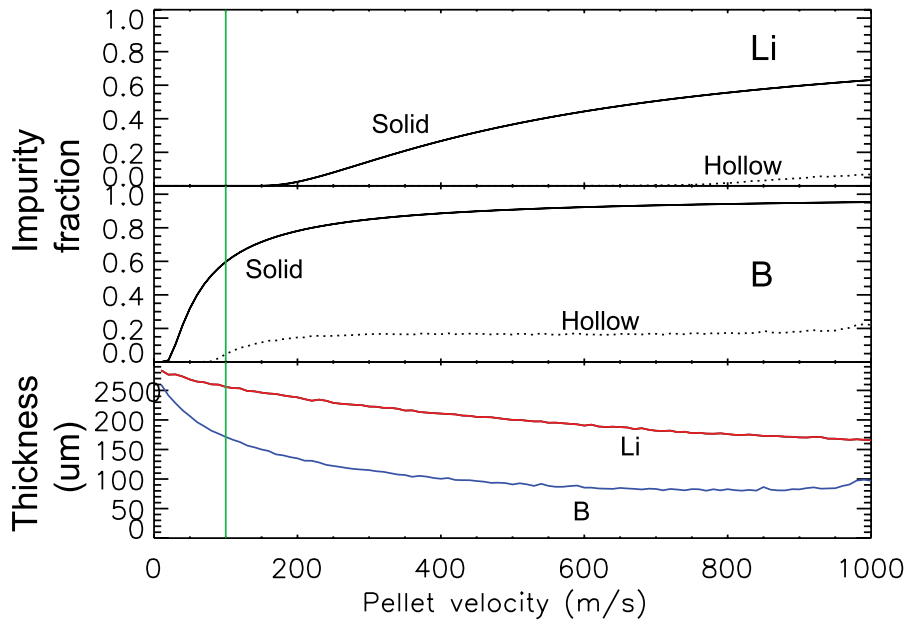


Figure 5. Impurity reduction using hollow pellets for a fixed initial pellet radius $r_p = 1$ mm and pedestal conditions as in figure 2. (Top) The fraction of the Li solid spheres (as shown in figure 4) and corresponding Li hollow spheres that reach beyond the ELM triggering location as a function of injection velocity. (Middle) The fraction of the B solid spheres (as shown in figure 4) and corresponding B hollow spheres that reach beyond the ELM triggering location as a function of injection velocity. (Bottom) The shell thicknesses of the hollow Li and B spheres chosen for different initial injection velocities by matching the peak dN/dr of the solid spheres with the corresponding hollow spheres. The colored vertical line corresponds to the example shown in figure 2.

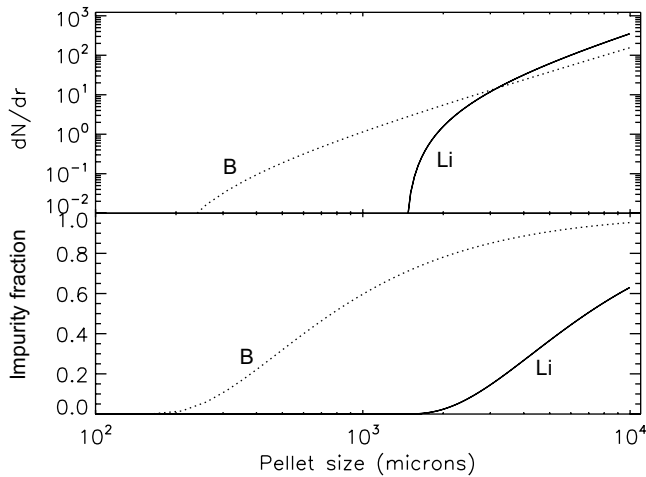


Figure 6. For a fixed pellet velocity $V_p = 100$ m s⁻¹ and fixed pedestal conditions as in figure 2, (top) the mass deposition (dN/dr in 10^{22} m⁻¹) as a function of Li or B solid sphere size (radius). (Bottom) The fraction of the solid spheres that reach beyond the targeted ELM triggering location as a function of solid sphere size.

Previous studies used several types of models for Δ : (a) constant Δ model [29–31], (b) Δ is proportional to r_p or $\kappa_2 r_p$ and that the multiplier (κ_2) is in the range of 2–10 [32–34], and the mixed model of (a) and (b) [35]. We use $\kappa_2 = 5$ here for illustration only, and a more comprehensive examination of the Δ -dependence of shell structures will be left to further studies. The smallest pellet that can satisfy all the conditions is therefore given by

$$r_p^{\min} = \frac{M_1}{\kappa_2 m_0 dN/dr} + T_h = \frac{N_{th}}{\kappa_2 dN/dr} + T_h \equiv T_1 + T_h, \quad (6)$$

where we introduce the *effective thickness* T_1 that directly contributes to ELM triggering. Using equation (1), T_1 can be expressed as in another form that is related to the pellet velocity v_p and dN/dt in equation (2),

$$T_1 = \frac{N_{th} v_p}{\kappa_2 dN/dt} = \frac{4\pi(r_p - T_h)^2 T_0 n_p v_p}{\kappa_2 dN/dt}. \quad (7)$$

Here we assume that, after going through the pre-triggering phase (ranging from the plasma edge to the triggering location), the residue hollow pellet is completely ablated in the ELM triggering location and therefore $M_3 = 0$. In addition, the residue mass or the number of particles is equivalent to the triggering threshold N_{th} or

$$N_{th} = \frac{4\pi}{3} n_p [(r_p - T_h)^3 - (r_p - T_h - T_0)^3] = 4\pi n_p (r_p - T_h)^2 T_0, \quad (8)$$

where we assume that the residue radius is $(r_p - T_h) \gg T_0$ (which is referred to as the *residue thickness* here) in both equations (7) and (8). The pellet density n_p is 4.44×10^{22} for Li and 1.39×10^{23} for B.

For the fixed pedestal condition as discussed above, T_h is found to be $158 \mu\text{m}$ (B) and $1424 \mu\text{m}$ (Li) respectively for $v_p = 100$ m s⁻¹. At $v_p = 400$ m s⁻¹, one finds the minimal B shell thickness to be $59 \mu\text{m}$ and the Li shell thickness to be $356 \mu\text{m}$. Additional results are summarized in figure 8. We find that $T_h \propto v_p^{-1}$. So higher injection velocities v_p correspond to less shell material loss before reaching the ELM triggering location, as expected. T_h is also found to be insensitive to r_p when r_p is sufficiently large.

For a fixed $N_{th} = 10^{19}$, 10^{20} and 10^{21} , the optimized pellet radius r_p^{\min} as a function of injection velocity is summarized

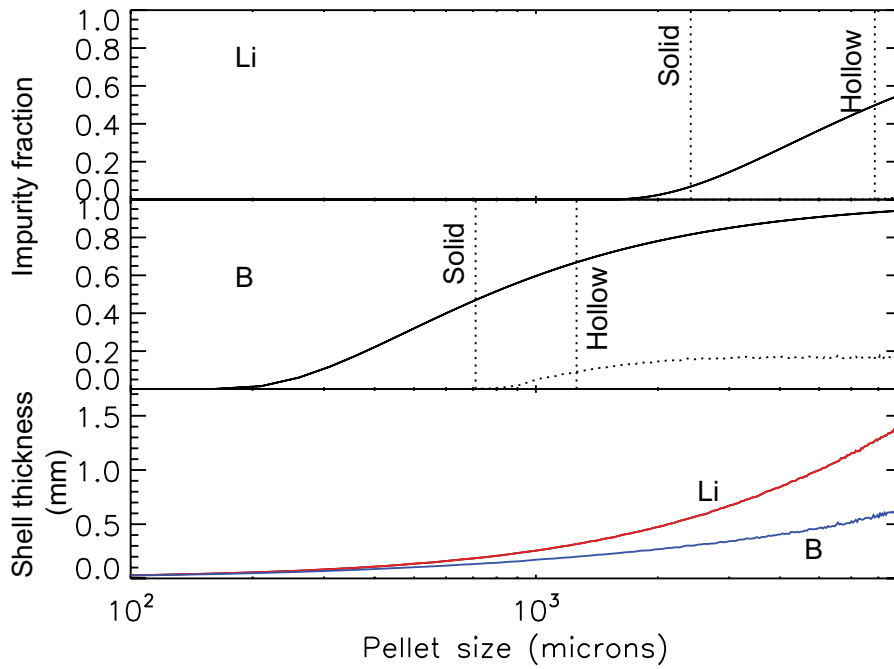


Figure 7. Using hollow pellets can extend the size ranges of the initial pellets without crossing the impurity threshold as given in figure 3. The plot is for a fixed initial pellet injection velocity $V_p = 100 \text{ m s}^{-1}$ and the same pedestal conditions as in figure 2. (Top) Li impurity fraction beyond the targeted ELM triggering location. The impurity limited pellet size increases from 2.41 mm for solid Li pellets to 6.86 mm for hollow Li pellets. (Middle) B impurity fraction beyond the targeted ELM triggering location. The impurity limited pellet size increases from 0.71 mm for solid B pellets to 1.26 mm for hollow B pellets. The vertical dashed lines in the top and middle frame illustrate the sizes as determined from the impurity limits.

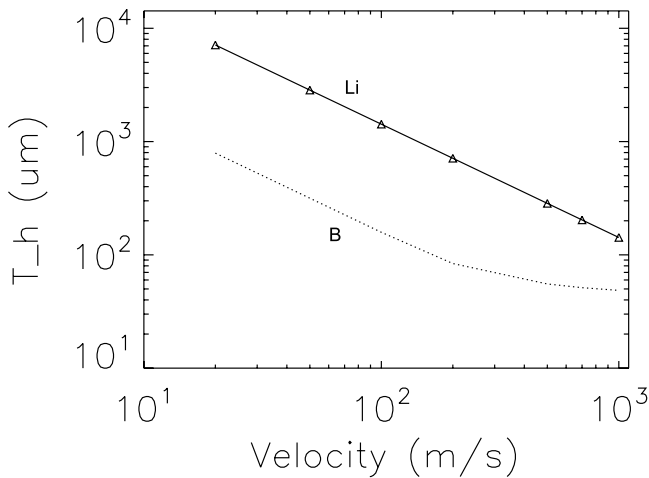


Figure 8. The shell thickness loss (defined as T_h) as a function of injection velocity (v_p) for Li and B pellets. The shell loss T_h is inversely proportional to v_p in most cases.

for Li and B in figure 9. Here we assume T_h is insensitive to the initial pellet size. Apparently, a larger pellet or mass is needed when N_{th} increases.

4. Hollow pellet fabrication

We briefly go through some existing options before summarizing the progress in developing hollow B spheres.

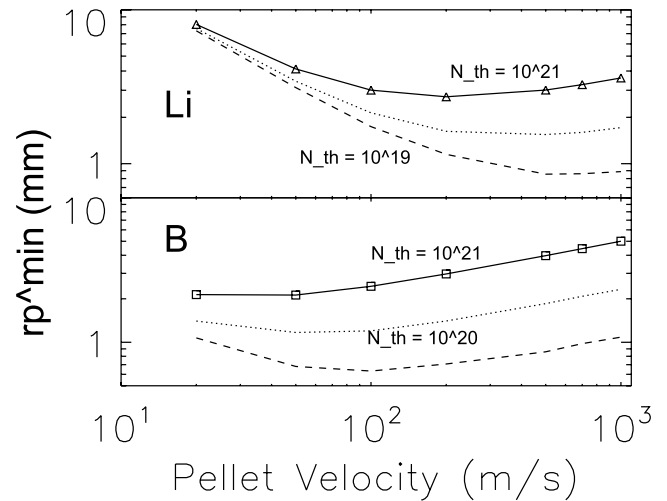


Figure 9. Optimal initial radius of hollow Li and B pellets (defined as r_p^{min}) as a function of the injection velocity for the same pedestal conditions as in figure 2. Three sets of curves for Li and B are for different N_{th} required at the pedestal shoulder (10^{19} —dashed lines, 10^{20} —dotted lines and 10^{21} —solid lines). The results also indicate that hollow pellet injection can be further optimized by tuning the injection velocity for the same N_{th} .

4.1. Existing options

Various hollow spherical targets have been developed for inertial confinement fusion (ICF) experiments [36–38]. Examples include hollow glass spheres, hollow polymer spheres (an

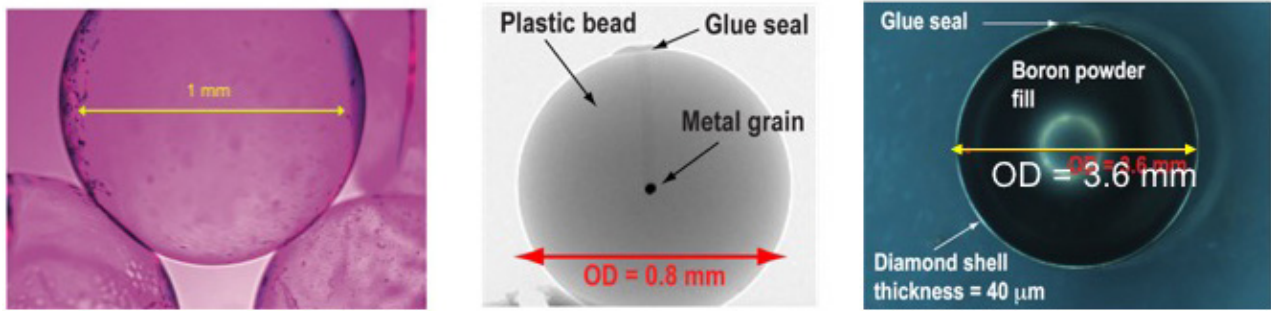


Figure 10. Examples of various core-shell pellets. (a) A hollow polymer pellet developed for ICF applications; the shell thickness is about $20\ \mu\text{m}$. (b) A plastic bead impregnated with a small tungsten grain, which is used as a calibration pellet in DIII-D; (c) a diamond shell filled with B powder. This is developed for disruption mitigation in DIII-D. The diamond shell thickness is $40\ \mu\text{m}$.

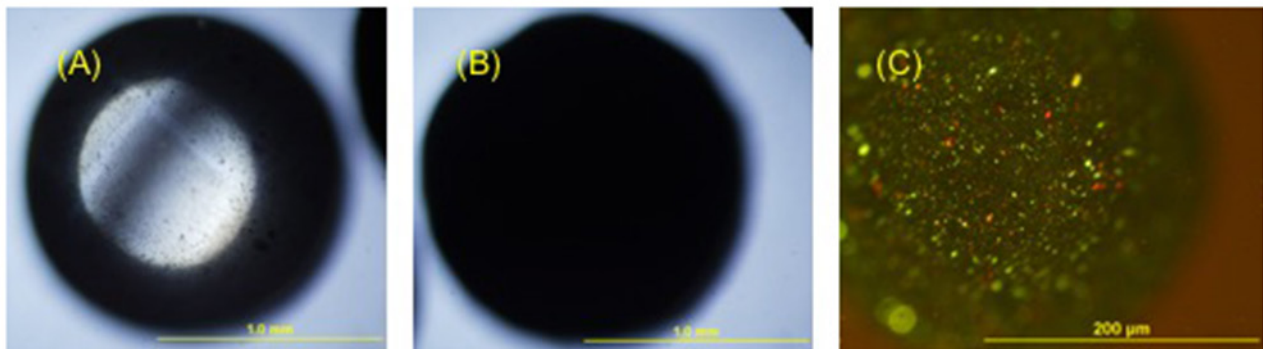


Figure 11. Optical microscope images of B-shell encapsulated PMMA spheres. (A) A PMMA sphere that is used as a template for B coating; the sphere is $1.5 \pm 0.05\ \text{mm}$ in diameter with a sphericity of $50\ \mu\text{m}$ according to the supplier. (B) A B-coated PMMA sphere; (C) the same sphere as in (B) with a higher microscope magnification. The scale bars are 1 mm in (A) and (B) and $0.2\ \text{mm}$ in (C).

example is shown in figure 10), and hollow boron carbide spheres. While some of these targets may be directly used in MF applications, broadening the material and structure choices is of interest for a number of reasons. The ICF targets are designed for DT fusion under extremely high pressure for a brief time window, which is estimated to be around $10^{-11}\ \text{s}$.

Core-shell spheres have also been developed and adopted in MF applications—see two examples shown in figure 10. Small hollow pellets are excellent tools for the calibration of spectroscopic diagnostics in tokamaks and stellarators like LHD [9, 39], as a well-known quantity of the desired material can be delivered to the plasma core. The shell protects the core material from ablation and loss in the launch tube and plasma edge region and ensures that the desired quantity of material to be studied reaches the core. In the DIII-D experiments [40], small ($\text{OD} = 0.8\ \text{mm}$) plastic (poly-alpha methylstyrene, PAMS, C_9H_{10}) bead pellets carrying much smaller ($10\ \mu\text{g}$) tungsten grains were used to calibrate the spectroscopic core tungsten measurements in support of the DIII-D tungsten divertor ring experiments. Another type of core-shell has also been pursued on the DIII-D tokamak for disruption mitigation studies [14].

We would like to point out some differences and commonalities between traditional ICF applications and the proposed new MF applications. Deployment of an ICF target does not involve significant motion or acceleration. Motion and acceleration could put additional requirements in the structural

rigidity. The key requirements in ICF hollow targets are the sphericity and uniform wall thickness of the shells. Impurity control is important for MF applications as mentioned above. Another unique feature of MF requirement is that the hollow sphere size may be larger. An ICF target is estimated to 1–2 mm in radius, constrained by the driver laser power and fusion power gain considerations.

4.2. B spheres

A growing number of methods are being developed to make spheres and hollow spheres, for example, microfluidic techniques [41]. We report the progress of hollow B shell development using an approach similar to a gel-casting method described recently to make boron carbide (B_4C) hollow spheres [42]. The fabrication consisted of two main steps. In the first step, core-shell structured B_4C was fabricated by coating molybdenum balls with B_4C slurry. The fabricated core-shell structured B_4C microspheres exhibit a large size ($2200\text{--}2300\ \mu\text{m}$) and a wall thickness of $100\text{--}180\ \mu\text{m}$. In the second step, the core-shell structured B_4C microspheres were laser drilled and the metal cores subsequently corroded to obtain the B_4C hollow microspheres. It should be mentioned that the gel-casting technique is also suitable for the preparation of other ceramic hollow microspheres that may be of interest to MF, including the assessment of material and first wall options. We have made the first samples of a B shell ($\sim 100\ \mu\text{m}$ thick) with

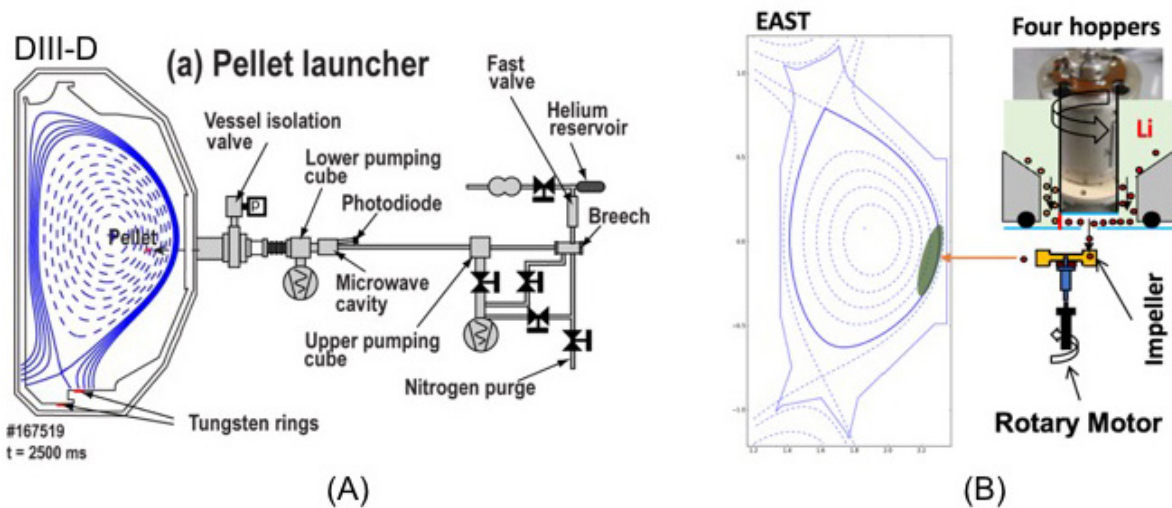


Figure 12. (A) Schematic of a pellet launcher used for various pellet injections in DIII-D. (B) Schematic of a four-hopper Li granule injector deployed on the EAST. This apparatus is able to inject four different sizes of pellets in the range of 0.2–1 mm. The velocity ranges from 30–110 m s⁻¹ for Li.

a polymethylmethacrylate (PMMA, acrylic) core (diameter 1.5 mm according to the supplier—Goodfellow item number ME306810), as shown in figure 11.

5. Experimental progress

Several existing techniques may be combined in the first hollow pellet experiments in MF. One is a pellet launching system. Another is a diagnostic system that can monitor the pellet–plasma interactions in real-time with good spatial and temporal resolutions. As the first example, a pneumatic (helium pulse) launcher in DIII-D can inject pellets radially inward at velocities of 100–300 m s⁻¹ from the outer mid-plane [40]. A schematic of the experimental setup is shown in figure 12. The pellet launcher breech is flexibly configurable to allow the holding and firing of different sized pellets.

Recently, the pneumatic launcher system was first successfully used to demonstrate the shell pellet concept for disruption mitigation in DIII-D [14]. A picture of the pellet used for this is shown in figure 10(c). The diamond shell had an OD of 3.6 mm and a shell thickness of 40 μm. The shell is filled with B powder. The pellet shells burnt through close to the plasma magnetic axis, releasing B powder and causing a very rapid radiative shutdown of the plasma, as shown in figure 13. Large hollow pellets (‘shell pellets’) filled with different payloads are of interest for tokamak disruption mitigation, since a precisely designed payload can be delivered to the plasma core and, ideally, satisfy the different shutdown requirements to minimize the different time-scales of wall damage that can result from disruptions, such as localized heat loads and vessel forces. Previous shell pellet disruption mitigation experiments have experienced challenges in getting payload deposition into the core during the disruption as the pellets have either passed completely through the plasma without breaking open, have broken in the plasma edge or have not caused a rapid shutdown [43]. Future work will continue to study the use of

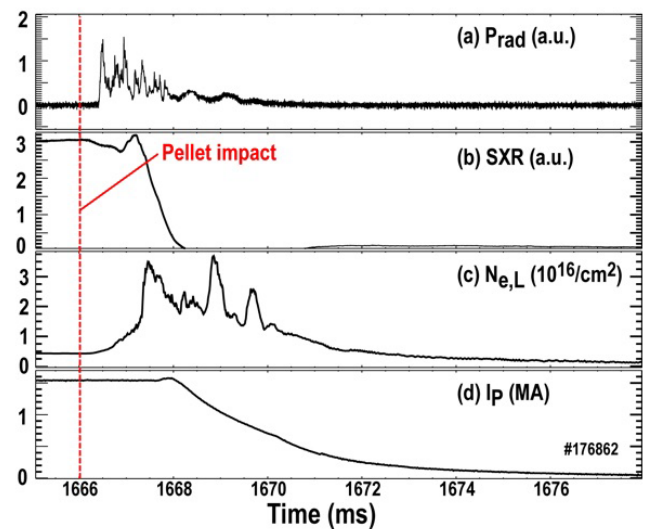


Figure 13. Example of rapid shutdown in DIII-D with a large (OD = 3.6 mm) shell pellet showing rapid radiative shutdown. Time traces are shown for (a) radiated power, (b) SXR brightness (showing the collapse of thermal energy), (c) electron line density (showing deposited impurities) and (d) plasma current (showing the decay of the magnetic energy).

shell pellets for disruption mitigation in DIII-D for application in future large tokamaks like ITER and DEMO.

EAST recently deployed a multi-chamber device to inject Li pellets with four different sizes for ELM pacing (see figure 12(B)), aiming at decoupling ELM triggering from the fueling effects of deuterium pellets [10]. By horizontally injecting Li pellets with velocities around 80 m s⁻¹, diameters ranging from 200 microns to 1 mm into the low field side of EAST H-mode discharges, it was demonstrated that Li pellets with diameters above 600 microns can successfully trigger ELMs more than 95% of the time [11]. When using 600 micron and larger solid Li pellets ($\sim 5.24 \times 10^{18}$ atoms), however, fueling of electron density was observed. Figure 14 shows

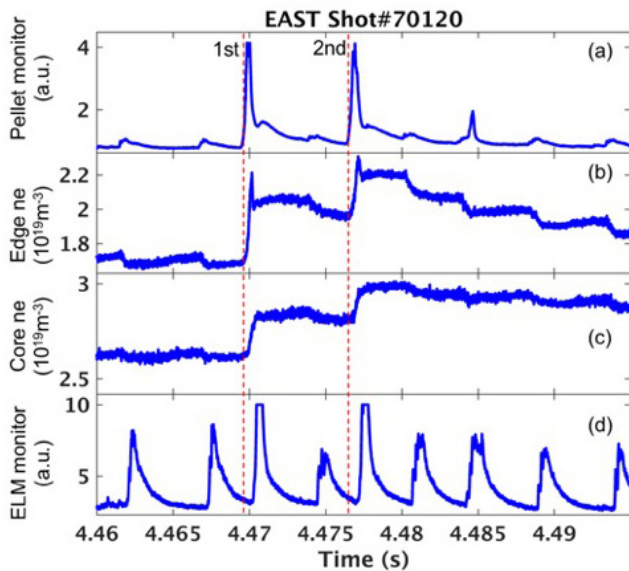


Figure 14. Typical two Li granule injection for ELM trigger on EAST. Time traces are shown for (a) granule injection monitor, (b) integrated density from edge chord and (c) core chord, and (d) D_{α} pointing to divertor for ELM monitor.

the typical 0.6mm Li pellets that are injected into H-mode plasma. The H-mode discharge with a plasma current of 400 kA was sustained by about 6 MW of auxiliary heating power. The average density is about $2.7 \times 10^{19} \text{ m}^{-3}$, maintained by feedback control via supersonic molecular beam injection. The two-pellet injection scheme produced sufficient edge plasma perturbation and triggered two ELMs, which was confirmed by the D_{α} spikes and edge density crash just following the pellet injection (the dashed lines in figure 14). Although the ELM crash caused an edge density reduction from 2.2 to 2.0, the edge density and core density were still $\sim 20\%$ higher than prior to the pellet injections. After the second pellet injection, the edge and core density rose further. The edge and core density reduced gradually by spontaneous ELMs. The core density reduction was slower than that of the edge density. These observations indicate that the pellet-triggered ELM cannot expel enough particles to maintain constant density in the plasma core. A large solid Li pellet, which is sufficient to trigger ELMs, cannot alleviate the fueling effect to the plasma core. Furthermore, increased radiation has also been observed correlated with Li pellet injection. The likely explanation is that the impurity ions from the pellet core likely contribute little to ELM triggering, but definitely to the electron density increase in the plasma core. Hollow pellets offer a promising method to solve this and the related issues.

For the *in situ* diagnostic of a hollow-pellet–plasma interaction, we may use a recently demonstrated dual-filter imaging technique [44]—the structure of pellet ablation is resolved using the new technique. The imaging technique can be used in conjunction with a hollow-pellet injection experiment.

6. Summary and conclusions

Precise delivery of mass to MF plasmas, particularly burning plasmas in ITER, is an area of growing interest. Existing and emerging applications include precision diagnostics, fueling, disruption mitigation, and ELM triggering and pacing. While extensive work has been dedicated to different mass delivery systems and different matter states, including gas, small atoms and clusters, dust, liquid jets, and solid pellets, new opportunities exist in the fabrication and utilization of precisely structured solid materials such as hollow or shell pellets. Our focus is on ELM triggering and pacing using hollow pellets, which shares similar theoretical techniques, modeling framework and possibly experimental techniques to their solid counterparts.

The main conclusion is that hollow pellets of Li or B can achieve similar ELM triggering effects to their solid counterparts, while significant plasma core contamination can be avoided or reduced to levels set by the dilution (for low-Z atoms) or radiation (for high-Z atoms) limits. The theoretical analysis is semi-analytical and one-dimensional. We do not include, for example, the effect of $\mathbf{E} \times \mathbf{B}$ polarization drift on the evolution of the ablation cloud. We first compare various empirical models for ablation and find the results are qualitatively similar. The hollow spherical pellet shell thickness and initial size depend on the injection velocity (v_p) as well as boundary plasma conditions and edge pedestal. When the plasma condition is fixed, the shell thickness can be reduced approximately as v_p^{-1} to achieve a similar ELM triggering effect, as measured by a certain number of atoms that are required near the top of a H-mode plasma pedestal. Prototype core–shell B spheres have been fabricated. Initial hollow pellet injection experiments in EAST and DIII-D are possible because of the recent progress and development in disruption mitigation and ELM experiments.

Follow-on work may be divided into three categories: more comprehensive theory and modeling, fabrication, and experimental demonstration. A fully integrated three-dimensional model of the hollow pellet injection, propagation, ablation and ELM triggering may require more sophisticated packages such as JOREK and BOUT++; these and others have been successfully used for the examination of plasma interactions with solid pellets. The hollow pellet concept may also be extended to other elements, including hollow pellets of LiD (suggested by an anonymous reviewer) or heavy elements such as tungsten. The fabrication of hollow pellets requires collaboration with the materials community. In addition to the reductive fabrication methods such as etching and machining, the new capabilities through additive manufacturing can offer new possibilities for the fabrication of hollow pellets. Initial hollow pellet injection experiments can use existing injectors developed for disruption mitigation and other applications. The injection of hollow pellets with very thin shells (below

10 s of micrometers with a diameter of at least several mm) may invite new accelerator technologies such as electrostatic injectors. Establishing hollow pellet injection as a routine method for MF energy, which is both attractive and challenging, as explained above, will necessitate the integration of efforts from the computation, materials, accelerators and MF community.

Acknowledgment

We thank Dr. Peter Goodwin (CINT/LANL) for help with the microscopy of boron spheres. LANL work is supported in part by the US Department of Energy (DoE) Fusion Energy Sciences long-pulse tokamak program through the Triad National Security, LLC ('Triad') contract # 89233218CNA000001. PPPL work is supported by US DoE through the contract # DE-AC02-09CH11466. DIII-D material is based upon work supported by US DoE under Award Number DE-FC02-04ER54698. This research is also partially funded by the National Key Research and Development Program of China (2017YFA0402500) and the National Natural Science Foundation of China (11625524).

Disclaimer

This report was prepared as an account of work sponsored by an agency of the United States Government. Neither the United States Government nor any agency thereof, nor any of their employees, makes any warranty, express or implied, or assumes any legal liability or responsibility for the accuracy, completeness, or usefulness of any information, apparatus, product, or process disclosed, or represents that its use would not infringe privately owned rights. Reference herein to any specific commercial product, process, or service by trade name, trademark, manufacturer, or otherwise, does not necessarily constitute or imply its endorsement, recommendation, or favoring by the United States Government or any agency thereof. The views and opinions of authors expressed herein do not necessarily state or reflect those of the United States Government or any agency thereof.

ORCID iDs

Zhehui Wang  <https://orcid.org/0000-0001-7826-4063>

Z. Sun  <https://orcid.org/0000-0002-7224-3592>

N.W. Eidietis  <https://orcid.org/0000-0003-0167-5053>

J.E. Menard  <https://orcid.org/0000-0003-1292-3286>

References

- [1] Zinkle S.J. *et al* 2014 *Fusion. Eng. Des.* **89** 1579–85
- [2] Federici G. *et al* 2001 *Nucl. Fusion* **41** 1967–2137
- [3] Naujoks D. 2006 *Plasma–Material Interaction in Controlled Fusion* (Berlin: Springer)
- [4] Wang Z. *et al* 2007 Physics of dust in magnetic fusion devices *New Aspects of Plasma Physics* (Singapore: World Scientific Publishing) pp 394–475
- [5] Loarte A. *et al* 2014 *Nucl. Fusion* **54** 033007
- [6] Maingi R. 2014 *Nucl. Fusion* **54** 114016
- [7] Wang Z. *et al* 2016 *J. Plasma Phys.* **82** 615820202
- [8] Lang P.T. *et al* 2004 *Nucl. Fusion* **44** 665–77
- [9] Sudo S. and Tamura N. 2012 *Rev. Sci. Instrum.* **83** 023503
- [10] Sun Z. *et al* 2018 *IEEE Trans. Plasma Sci.* **46** 1076
- [11] Lunsford R. *et al* 2018 *Nucl. Fusion* **58** 126021
- [12] Lang P.T. *et al* 2011 *Nucl. Fusion* **51** 033010
- [13] Huijsmans G.T.A. *et al* 2015 *Phys. Plasmas* **22** 021805
- [14] Hollmann E.M. *et al* 2019 *Phys. Rev. Lett.* **122** 065001
- [15] Rozhansky V. *et al* 2004 *Plasma Phys. Control. Fusion* **46** 575
- [16] Pégourié B. 2007 *Plasma Phys. Control. Fusion* **49** R87
- [17] McCarthy K.J. *et al* 2017 *Europhys. Lett.* **120** 25001
- [18] Parks P.B. *et al* 1988 *Nucl. Fusion* **28** 477
- [19] Yu S.V. *et al* 2006 *Plasma Phys. Rep.* **32** 398–412
- [20] Snyder P.B. *et al* 2002 *Phys. Plasma.* **9** 2037
- [21] Xu X.Q. *et al* 2010 *Phys. Rev. Lett.* **105** 175005
- [22] Xi P.W. *et al* 2014 *Phys. Rev. Lett.* **112** 085001
- [23] Huysmans G.T.A. *et al* 2009 *Plasma Phys. Control. Fusion* **51** 124012
- [24] Futatani S. *et al* 2014 *Nucl. Fusion* **54** 073008
- [25] Wang Y.M. 2018 private communication
- [26] Kocsis G. *et al* 2007 *Nucl. Fusion* **47** 1166–75
- [27] Ceccil J.L. 1980 *J. Nucl. Mater.* **93** and **94** 28–43
- [28] Wang Z. and Kline J. 2003 *Appl. Phys. Lett.* **83** 1662
- [29] Lengyel L.L. 1988 *Phys. Fluids* **31** 1577
- [30] Pégourié B. *et al* 1993 *Nucl. Fusion* **33** 591
- [31] Garzotti L. *et al* 1993 *Nucl. Fusion* **37** 1167
- [32] Kaufmann M. *et al* 1986 *Nucl. Fusion* **26** 171
- [33] MacAulay A.K. 1994 *Nucl. Fusion* **34** 43
- [34] Polevoi A.R. and Shimada M. 2001 *Plasma Phys. Control. Fusion* **43** 1525
- [35] Houlberg W.A. *et al* 1988 *Nucl. Fusion* **28** 595
- [36] Hoppe M. 2000 *Fusion Technol.* **38** 42
- [37] Nagai K. *et al* 2004 *J. Plasma Fusion Soc.* **80** 626
- [38] Du K. *et al* 2018 *Matt. Rad. Extr.* **3** 135
- [39] Tamura N. *et al* 2015 *Plasma Fusion Res.* **10** 1402056
- [40] Hollmann E.M. *et al* 2017 *Rev. Sci. Instrum.* **88** 103501
- [41] Nisisako T. 2016 *Curr. Opin. Colloid Interface Sci.* **25** 1
- [42] Chen R. *et al* 2017 *Ceram. Int.* **43** 571
- [43] Hollmann E.M. *et al* 2010 *Phys. Plasmas* **17** 056117
- [44] Sun Z. 2018 *et al* *Rev. Sci. Instrum.* **89** 10E112